buildings

MDPI

Article

Numerical Analysis of Reinforced Concrete Corbels Using Concrete Damage Plasticity: Sensitivity to Material Parameters and Comparison with Analytical Models

Ygor Moriel Neuberger [1,*], Maykon Vinicius Andrade [1], Alex Micael Dantas de Sousa [2], Mariana Bandieira [1], Edivaldo Pereira da Silva Júnior [3], Herisson Ferreira dos Santos [3], Bruna Catoia [1], Emerson Alexandro Bolandim [4], Vinicius Borges de Moura Aquino [4], André Luis Christoforo [1] and Marcelo de Araújo Ferreira [1]

[1] Department of Civil Engineering, Federal University of Sao Carlos, Sao Carlos 13565-905, Sao Paulo, Brazil; maykon@estudante.ufscar.br (M.V.A.); marianabandieira@gmail.com (M.B.); bcatoia@ufscar.br (B.C.); alchristoforo@ufscar.br (A.L.C.); marcelof@ufscar.br (M.d.A.F.)
[2] Sao Carlos Engineering School, University of Sao Paulo, Sao Carlos 13566-590, Sao Paulo, Brazil; alex_dantas@usp.br
[3] Federal Institute of Rondonia, Campus Ariquemes, Ariquemes 76870-000, Rondonia, Brazil; edivaldo.pereira@estudante.ifro.edu.br (E.P.d.S.J.); herisson.santos@ifro.edu.br (H.F.d.S.)
[4] Department of Civil Engineering, Universidade Estadual Paulista (UNESP), Ilha Solteira 15385-000, Sao Paulo, Brazil; emerson.bolandim@unesp.br (E.A.B.); vinicius.bm.aquino@unesp.br (V.B.d.M.A.)
* Correspondence: ygor.neuberger@estudante.ufscar.br

check for updates

Citation: Neuberger, Y.M.; Andrade, M.V.; de Sousa, A.M.D.; Bandieira, M.; da Silva Júnior, E.P.; dos Santos, H.F.; Catoia, B.; Bolandim, E.A.; de Moura Aquino, V.B.; Christoforo, A.L.; et al. Numerical Analysis of Reinforced Concrete Corbels Using Concrete Damage Plasticity: Sensitivity to Material Parameters and Comparison with Analytical Models. *Buildings* **2023**, *13*, 2781. https://doi.org/10.3390/buildings13112781

Academic Editor: Francisco López-Almansa

Received: 3 October 2023
Revised: 20 October 2023
Accepted: 30 October 2023
Published: 5 November 2023

Abstract: The Concrete Damage Plasticity (CDP) model is a widely used constitutive model to represent the non-linear behavior of concrete in numerical analysis. However, a limited number of studies compared the level of accuracy of numerical models with the main code provisions from the literature. In addition, the influence of CDP material parameters on the structural behavior of corbels was scarcely studied. This study proposes to evaluate the ability of numerical models using CDP to represent the structural behavior of corbels regarding the ultimate load, reinforcement deformation and failure mechanism. In addition, we compared the predictions of the numerical models with the ones from design code expressions regarding the ultimate capacity. For this, three test results of corbels from the literature were evaluated with numerical models using the CDP, as well as with analytical models from different code provisions. A sensitivity analysis—by changing the dilation angle (ψ) and shape factor (K_c)—was performed. The comparison between tested and predicted resistances with the proposed numerical modeling choices was equal to 1.04 with a coefficient of variation of 11%. On the other hand, the analytical models evaluated overestimated the corbel capacity by more than 62%, on average. Therefore, the proposed modeling choices provide better predictions of ultimate capacity than the evaluated analytical models and can be used to assess the corbel design under more complex boundary conditions.

Keywords: reinforced concrete corbels; numerical modeling; concrete damage plasticity (CDP); region of stress discontinuity (D region)

1. Introduction

Corbels are three-dimensional reinforced concrete structures that serve as beam–column connection elements and are widely used in the precast structures industry. National and international standards and regulations, such as ABNT NBR 9062:2017 [1], PCI [2] and EN 1992-1-1:2004 [3], provide analytical models for designing corbels that, in general, they are methods derived from strut and tie models and friction-shear models.

To understand the behavior of corbels, several authors [4–13] conducted laboratory tests on these elements to assess how concrete strength (f_c), main reinforcement, secondary

reinforcement (stirrups and links) and geometry influence the corbel's behavior in terms of failure mode and ductility. Based on these results, analytical models were developed and calibrated.

Araújo et al. [14] analytically compared a database with 62 short concrete corbels using normative models [1–3] and observed low accuracy of the analytical models in predicting the experimental failure strength, with an average ratio $V_{u.exp}/V_{u,ana}$ between 0.83 and 1.30 and a high coefficient of variation (COV) between 31% and 59%. One of the explanations for these results is that corbels are elements from region D. According to Szczecina and Winnicki [15], elements from region D represent a region of stress discontinuity, where the distribution of deformations is not linear. This may explain the difficulty of analytical models in accurately predicting the experimental result of corbels, especially when failure occurs in the strut, which is a region of stress disturbance.

Numerical models based on the Finite Element Method (FEM) are useful for studying D regions as they allow evaluation of the behavior of structural elements subjected to a three-dimensional stress field. However, to correctly predict results, the computational model must adequately represent the non-linear behavior of materials, especially concrete.

Several authors [16–20] used numerical modeling software, such as Ansys®, Atena® and Diana®, to evaluate concrete corbels and obtained a good representation when comparing numerical and experimental results. Canha [18] modeled 100 corbels from the literature using Atena® and obtained an average ratio $V_{u.exp}/V_{u,num}$ of 1.03, with a COV of 15.9%. However, no similar works were found using the Abaqus® software and CDP (Concrete Damage Plasticity) in the evaluation of corbels.

The objective of this work is to present a numerical modeling strategy for short reinforced concrete corbels using CDP, validated through comparison with experimental results regarding the ultimate strength and deformations of the reinforcement. Furthermore, we intend to discuss and evaluate the influence of some CDP parameters on the structural behavior of the corbels. Finally, the results of computational modeling were compared with those obtained by analytical models [1–3]. In this way, we intend to illustrate the potential of using numerical models to evaluate short corbels in future studies under more complex boundary conditions.

2. CDP Model (Concrete Damage Plasticity) on ABAQUS

In this study, the Concrete Damage Plasticity (CDP) model from ABAQUS® [21] was employed to describe the concrete non-linear behavior.

The CDP was developed by Lubliner et al. [22], with improvements made by Lee and Fenves [23].

The CDP model combines characteristics of two main phenomena: damage and plasticity. The damage considers the degradation of the modulus of elasticity (E) with the development of cracks and microcracks in the concrete, which can occur due to the application of high loads or events such as impacts or repetitive load cycles. Plasticity is related to the development of permanent or irreversible deformations of concrete (also called plastic deformations), even after the removal of the load [24,25].

In the CDP model, the concrete response is represented through state variables that describe the level of damage and accumulated plasticity for a given level of stress and deformation. These variables are updated according to specific rules defined in the model. The CDP considers five input variables—expansion angle (ψ), eccentricity (e), the relationship between biaxial/axial stress (σ_{b0}/σ_{c0}), the rate of the second stress invariant or shape factor (K_c) and viscosity (μ)—in addition to the uniaxial tension–strain curves for tension and compression ($\sigma_c \times \varepsilon_c$ and $\sigma_t \times \varepsilon_t$) and damage evolution curves ($d_c \times \varepsilon_c$ and $d_t \times \varepsilon_t$), to calculate the evolution of plastic and inelastic stresses and deformations of concrete [26].

Detailed descriptions of the CDP model and identification of its parameters can be found in the following references [24–29]. The model was formulated based on the following characteristics of the concrete:

2.1. Stress–Strain Relationship

In the CDP model, stiffness degradation is modeled based on the definition of the relationship between effective stress and damage. The stress–strain model obtained in CDP is based on a simple model that delivers the relationship between damage and plasticity using scalar damage and effective stress, as shown in Equation (1) [29].

$$\sigma = (1-d){D_0}^{el} : (\varepsilon - \varepsilon^{pl}) = (1-d)\overline{\sigma} \quad (1)$$

where σ is Cauchy stress; ${D_0}^{el}$ is the initial elastic stiffness (without damage); ${D^{el}} = (1-d){D_0}^{el}$ is the damaged elastic stiffness; ε is total strain; ε^{pl} is the plastic strain; indicates Frobenius inner product; and d is the damage variable, which may vary from zero (material without damage) to a fully damaged material [30]. According to the concept of effective stress, the plastic yield function is formulated in terms of the effective stress, σ.

2.2. Hardening Variables

Damaged states of tension and compression are considered by two hardening variables, $\tilde{\varepsilon}_t^{pl}$ e $\tilde{\varepsilon}_c^{pl}$, referring to the equivalence of plastic traction and compression, respectively. Micro-cracking in concrete is represented by an increase in the values of the hardening variables [21].

2.3. Yield Criteria

The function of the yield surface (Figure 1a) is based on the model proposed by [10,11]. The flow functions follow the Kuhn–Tucker condition and lead to the following formula in the space for effective stress [31]:

$$F = \frac{1}{1-\alpha}(\overline{q} - 3\alpha\overline{p} + \beta(\tilde{\varepsilon}^{pl})(\overline{\sigma}_{\max})) - \gamma(\overline{\sigma}_{\max})) - \overline{\sigma}_c(\tilde{\varepsilon}_c{}^{pl}) \quad \leq \quad 0 \quad (2)$$

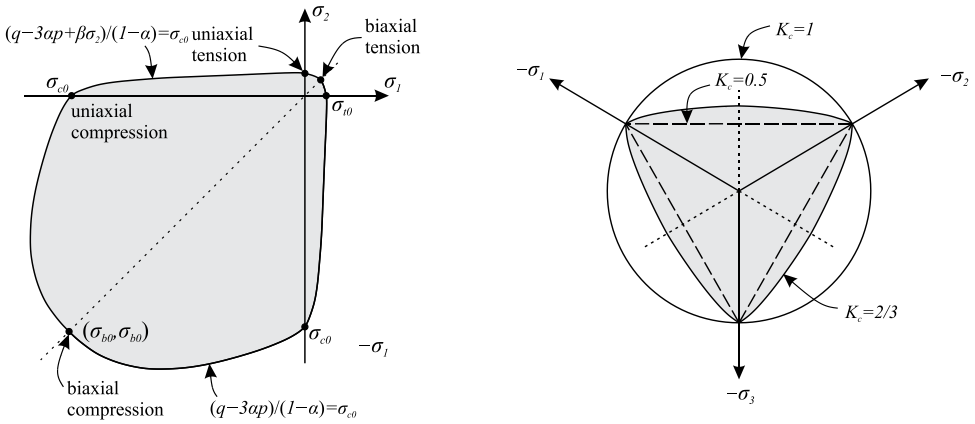

Figure 1. Representation of failure surfaces in the CDP Model: (**a**) Yield surface in the stress plane; (**b**) Yield surface in the deviatoric plane. Adapted from Reginato et al. [30].

$\overline{p}$ is the effective hydrostatic pressure; $\overline{q}$ is the von Mises equivalent stress; (x) = 0.5(x + | x |) is the Macaulay bracket; $\overline{\sigma}_{\max}$ is the algebraically maximum eigenvalue of the tensor $\overline{\sigma}_c$; and α, β e γ are dimensionless constants, which are defined in Equations (3)–(5), respectively.

$$\alpha = \frac{(\sigma_{b0}/\sigma_{c0}) - 1}{2(\sigma_{b0}/\sigma_{c0}) - 1} \rightarrow 0 \leq \alpha \leq 0.5 \quad (3)$$

$$\beta(\tilde{\varepsilon}^{pl}) = \frac{\overline{\sigma}_c(\tilde{\varepsilon}_c{}^{pl})}{\overline{\sigma}_t(\tilde{\varepsilon}_t{}^{pl})}(1-\alpha) - (1+\alpha) \quad (4)$$

$$\gamma = \frac{3(1 - K_c)}{2K_c - 1} \tag{5}$$

It is worth mentioning that the parameters α, β and γ are parameters with physical meaning and can be determined experimentally based on uniaxial, bi-axial and triaxial tests of concrete. However, as confined tests (biaxial and triaxial) require more complex equipment, these tests are only carried out in more specific studies. For this reason, most of the time, the parameters that define the biaxial and triaxial behavior of concrete are determined by calibrating numerical models.

$_{b0}/\sigma_{c0}$ is the ratio between the biaxial compression and the uniaxial compression yield stress that influences the yield surface in a state of full tension. Typical experimental values of the ratio σ_{b0}/σ_{c0} range between 1.10 and 1.16 [32–34]; $\overline{\sigma}_c(\widetilde{\varepsilon}_c{}^{pl})$ e $\overline{\sigma}_t(\widetilde{\varepsilon}_t{}^{pl})$ are the effective cohesion stress in compression and tension, respectively. The coefficient γ appears only in triaxial compression stress states. This factor can be determined by comparing yield conditions along the tensile and compression meridians. The parameter K_c is the coefficient that defines the shape of the deviatoric cross-section, as shown in Figure 1b.

2.4. Flow Rule

The concrete stress–strain relationship and the yield surface are connected using the flow rule. The CDP model assumes the unassociated hyperbolic Drucker–Prager function for the flow potential function, *G*, as expressed in Equation (6).

$$G = \sqrt{(\varepsilon\sigma_{t0}\tan\psi)^2 + \overline{q}^2} - \overline{p}\tan\psi \tag{6}$$

where ε is the potential flow eccentricity, σ_{t0} is the uniaxial tensile stress and ψ is the dilation angle. Poliotti and Bairán [35] explain that dilatancy can be described as the volume change of a granular material submitted to shear strains. Experimentally, the dilation angle can be determined with the results from triaxial compressive tests [36]. In practice, the dilation angle controls the evolution of the transverse strain under axial stresses after cracking. Based on this, the dilation angle tends to play a significant influence on problems subjected to high confining stresses, as restrained transverse strains may increase uniaxial concrete strength.

2.5. Viscoplastic Regularization

Materials that exhibit softening behavior and stiffness degradation can result in solution convergence problems during the processing of numerical models. To overcome some of these difficulties, viscoplastic regularization of the constitutive model was implemented in CDP with the viscosity parameter (μ). The default value of the ABAQUS® viscosity parameter is zero, which means that no viscoplastic adjustment is performed. Therefore, viscosity is a parameter defined only numerically to reduce convergence problems and has no physical meaning (it cannot be obtained experimentally, for example). In practice, the viscosity value must be chosen with caution so as not to result in changes in structural behavior.

In short, to use the CDP model in ABAQUS®, you must inform the two uniaxial stress–strain relationships or curves (tension and compression—$\sigma_c \times \varepsilon_c{}^{in}$ e $\sigma_c \times \varepsilon_t{}^{in}$), two relationships/damage evolution curves (traction and compression—$\varepsilon_c{}^{in} \times d_c$ e $\varepsilon_t{}^{in} \times d_t$) and five additional parameters to define the biaxial and triaxial behavior of the concrete. Four values are given for stress–strain in compression and tension and damage parameters in tension and compression. The five additional parameters are the values to define the flow surface (σ_{b0}/σ_{c0} e K_c), potential flow (ψ e e) and viscoplastic regularization (μ).

3. Experimental Models

To validate the computational model with CDP, three specimens of short corbels tested in the laboratory and available in the literature [9–11] were used. Table 1 presents the

mechanical and geometric characteristics necessary to create the computational model, in addition to the resistance associated with the yielding of the tie reinforcement (V_y) and rupture of the connecting rod concrete (V_u) in each corbel. In Table 1, f_c is the uniaxial compressive strength of the concrete, f_y indicates the yield stress of the tie reinforcement, f_{ys} is the yield stress of the seam reinforcement and w_p is the width of the corbel reaction plate. From Table 1, two classes of concrete were evaluated in the study: (i) normal strength concrete (f_c < 50 MPa in Araújo et al. [10] and Fattuhi and Hugles [11]) and (ii) concrete high resistance (f_c = 75.3 MPa in Fernandes [9]). In practice, high-strength concrete tends to exhibit more brittle behavior upon failure.

Table 1. Mechanical and geometric properties of short corbels [9–11].

Reference	Corbels	$V_{y,exp}$ (kN)	$V_{u,exp}$ (kN)	Geometry					
				a/d	*a* (mm)	*h* (mm)	*b* (mm)	*d* (mm)	*d′* (mm)
Fernandes [9]	FE-CS6-4A	120	160	0.57	60	120	120	105	15
Araújo et al. [10]	M3-MONO-A	248	314.4	0.63	225	400	200	360	40
Fattuhi e Hugles [11]	FA-T8	188.4	188.4	0.68	89	150	150	130	20

		f_c (MPa)	Tie reinforcement			Seam reinforcement			
			ϕ_l (mm)	A_s (mm^2)	f_y (MPa)	ϕ_t (mm)	A_{sf2} (mm^2)	f_{ys} (MPa)	*wp* (mm)
Fernandes [9]	FE-CS6-4A	75.3	6.3	125	525	4.2	55	750	50
Araújo et al. [10]	M3-MONO-A	43.09	12.5	245	670	6.3	187	615	50
Fattuhi e Hugles [11]	FA-T8	44.62	12	226	491	10	314	558	50

Figure 2 shows the test scheme, in which the double console is positioned inverted to facilitate the laboratory arrangement. The specimen is bi-supported with first and second-gender supports on the corbels to guarantee staticity and simulate the real behavior of the structure. In all tests, displacement control was applied to the upper face of the column, which makes it possible to capture the post-peak section in the load × displacement curve.

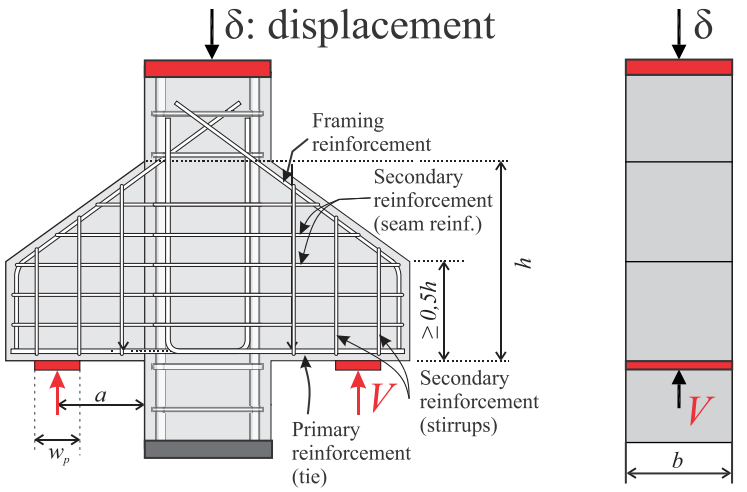

Figure 2. Geometric characteristics and test scheme of selected corbels.

4. Computational Model

The three-dimensional computational model was created in the Abaqus® software, respecting the geometry, quantity and positioning of the reinforcement, according to the models tested by the authors [9–11].

Reduced integration hexaedric cubic elements of type C3D8R were used to represent the concrete and loading plates. Furthermore, T3D2-type truss elements were used to simulate all the model's reinforcement.

The reinforcements were modeled considering the non-linearity of the steel (hardening) and perfect adhesion with the surrounding concrete (embedded formulation). The simplification of considering a perfect bond between concrete and reinforcement is based on the absence of anchorage failure at the tests. In addition, the influence of small sliding at the concrete–reinforcement interface is limited for such problems [30]. In practice, one of the minor shortcomings of such simplification is that the load-deflection response from the numerical models tends to show a stiffer behavior.

For the concrete, the Concrete Damage Plasticity (CDP) constitutive model was used. Welded connections (tie) were considered between the concrete parts and the loading and reaction plates. The loading and supporting plates were modeled considering the thickness and dimensions of the plate used in the test and material with linear-elastic behavior, as the stress concentration in the plates is much lower than the yield stress of the material.

The constitutive models for steel and concrete, as well as the mesh refinement analysis, will be explained below.

4.1. Steel Constitutive Model

To represent the steel, an elastoplastic constitutive model with linear hardening was used. The bi-linear stress–strain curve of the steel was provided directly in the software, which is conducted by informing the stress and the respective plastic deformation of the material. The modulus of elasticity (E_s) equal to 200 GPa was used, the Poison coefficient (v) equal to 0.3, the plastic strain equivalent to yielding is equal to zero, and the plastic strain equivalent to rupture is equal to $0.01\varepsilon_y$, where ε_y represents the yielding strain of the steel.

4.2. Concrete Constitutive Model

Table 2 specifies the parameter values used in this modeling to represent the non-linear behavior of concrete. At this first moment, the CDP parameters used were those recommended by the standard for eccentricity (e), the relationship between biaxial and uniaxial tension (σ_{b0}/σ_{c0}), viscosity (μ) and shape factor (K_c). The dilation angle (ψ) usually varies between 30° and 42° [24] and will be the target of the sensitivity study. However, to carry out the first numerical model and the sensitivity analysis of the mesh, the value of 30° was used.

Table 2. Constitutive laws and definitions of concrete material in Abaqus® software.

Material Elastic Properties	
Modulus of elasticity (E_c):	$E_c = 22\left(\frac{f_c}{10}\right)^{0.3}$ [a]
Poisson coefficient (v):	$v = 0.2$ [a]
CDP Parameters	
Dilation angle (ψ):	30
Eccentricity (e):	0.1 [b]
Relation between bi-axial and uniaxial stress (σ_{b0}/σ_{c0}):	1.16 [b]
Shape factor (K_c):	0.667 [b]
Viscosity (μ):	0.0005 [c]
Stress–Strain Curves	
Compression	Carreira e Chu [37]
Tension	Genikomsou e Polak [29]
Damage Evolution Law	
Compression	Yu et al. [38]: ($d_c = 1 - \sigma_c/f_c$)
Tension	Yu et al. [38]: ($d_t = 1 - \sigma_{ct}/f_{ct}$)

[a] Values recommended by EN 1992-1-1:2004 [3]; [b] Recommended default values [12]; [c] Arbitrated value to assist in convergence.

Figure 3a presents the curve proposed by Carreira and Chu [37] that was used in this work to represent the compression behavior of concrete. The compression strain (ε_{c1}) associated with the maximum compression stress f_c was calculated in accordance with EN 1992-1-1:2004 [3]. Figure 3b,c shows the stress–strain curve adapted from Genikomsou and Polak [29], which was used to represent the behavior of concrete in tension. The concrete fracture energy (Gf) was calculated according to the CEB-FIP Model Code [39].

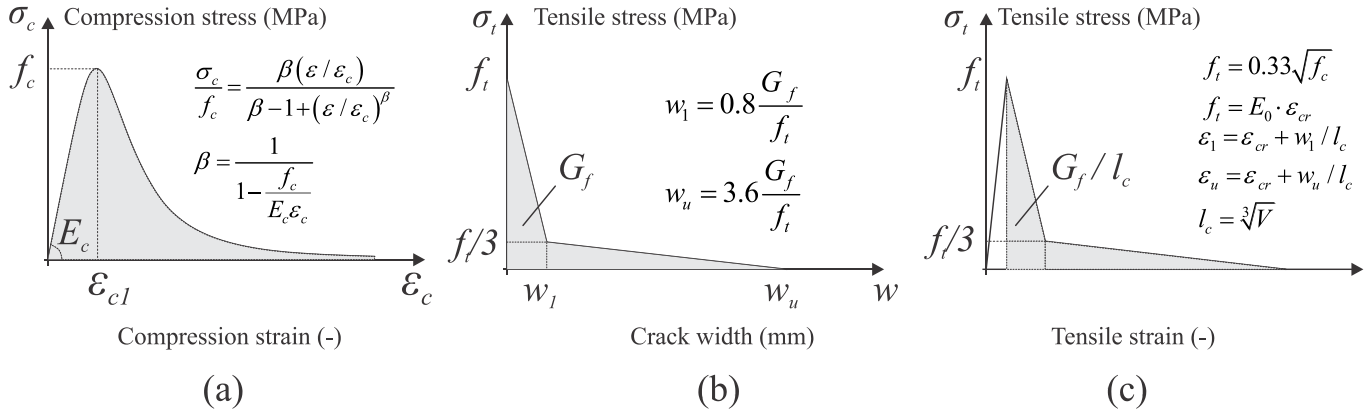

Figure 3. Concrete constitutive laws for tension and compression. Adapted from [29,37]: (**a**) Compression concrete; (**b**) Tensile behavior: stress × crack opening; (**c**) Tensile behavior: stress × strain.

5. Mesh Refinement

Aiming to perform the sensitivity analysis of the mesh, we chose to use the M3-MONO-A specimen with intermediate geometry, i.e., a/d ratio = 0.625, tested by Araújo et al. [10]. Information about the geometric and material properties of this corbel is found in Table 1. Figure 4a shows the geometry of the numerical model created. Two reference points were created to apply the boundary conditions and monitor the results: (i) RP-1 on the upper face of the column, in the center of the loading plate, where displacement control was implemented and reactions are measured; and (ii) RP-2 in the lower central region of the column, where vertical displacements are measured. In Figure 4b, the positioning and arrangement of reinforcement used is presented.

The mesh refinement analysis was based on three main parameters: finite element size, processing time and crack distribution. Changing the size of the finite element directly influences the accuracy and quality of the response. Furthermore, the smaller the finite element, the longer the processing time. Table 3 presents the results obtained from the five meshes that were tested.

The best approximations to the experimental results regarding corbel resistance ($V_{u,exp}$) were obtained with 25 mm and 35 mm meshes, as can be seen in Figure 5a. Figure 5b displays the tensile damage for the peak load in each analyzed mesh. The best approximations of the crack pattern were obtained in the 15 mm and 25 mm meshes. Due to the consistency with the results of the more refined mesh (10 mm) and the low processing time, the 25 mm mesh was chosen as the standard mesh for this console. The result obtained reached $V_{u,num}/V_{u,exp}$ of 0.92, with a processing time of just 21 min. In general, the most significant difference between the experimental and numerical curves in the evolution of displacements can be related to (i) accommodations in the support system not considered in the numerical modeling, (ii) the assumption of no concrete micro-cracking at the initial loading and (iii) the assumption of the perfect bond between reinforcement and concrete. However, the ultimate strength and rupture mechanism of the tests were well represented by numerical models, which are the most important parameters in the ultimate limit state.

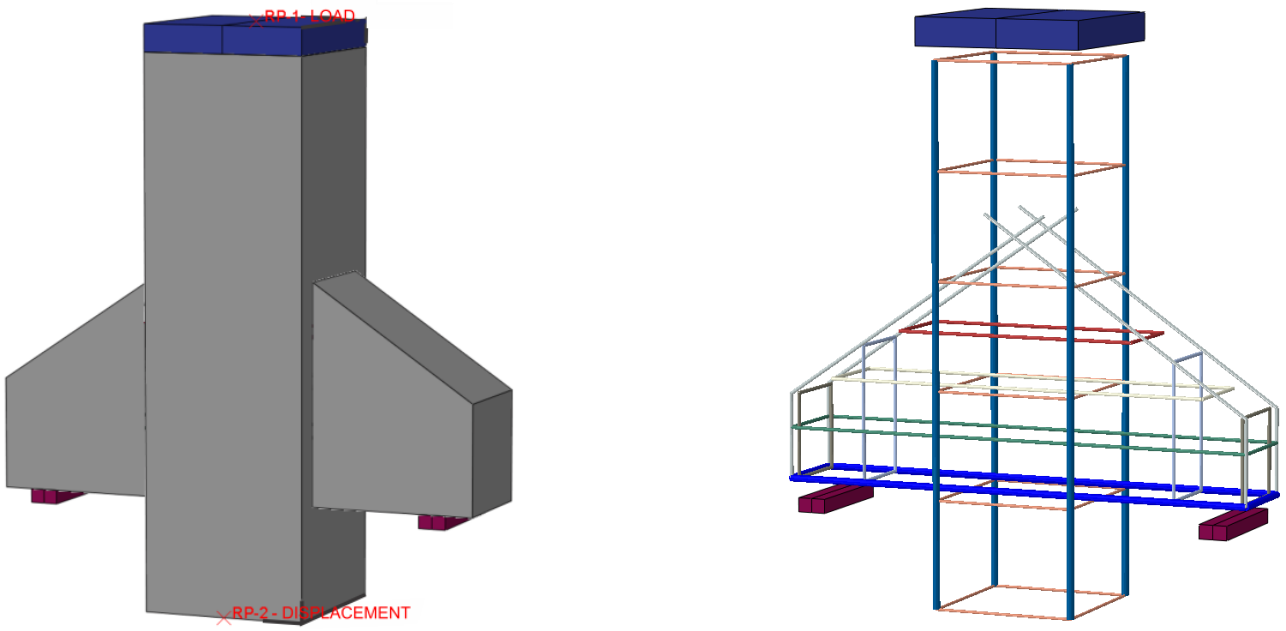

(**a**) (**b**)

Figure 4. Specimen model M3-MONO-A created in Abaqus®: (**a**) Corbel and loading plates; (**b**) Tie and seam reinforcement.

Table 3. Mesh refinement analysis.

Test	Interpolation Order	Average Element Size [mm]	Hexaedric Solid Element	Linear Element	Processing Time [min]	$\frac{V_{u,num}}{V_{u,exp}}$
1	Linear	10	C3D8R	T3D2	658	0.86
2	Linear	15	C3D8R	T3D2	228	0.89
3	Linear	25	C3D8R	T3D2	21	0.92
4	Linear	35	C3D8R	T3D2	14	0.94
5	Linear	50	C3D8R	T3D2	5	0.87

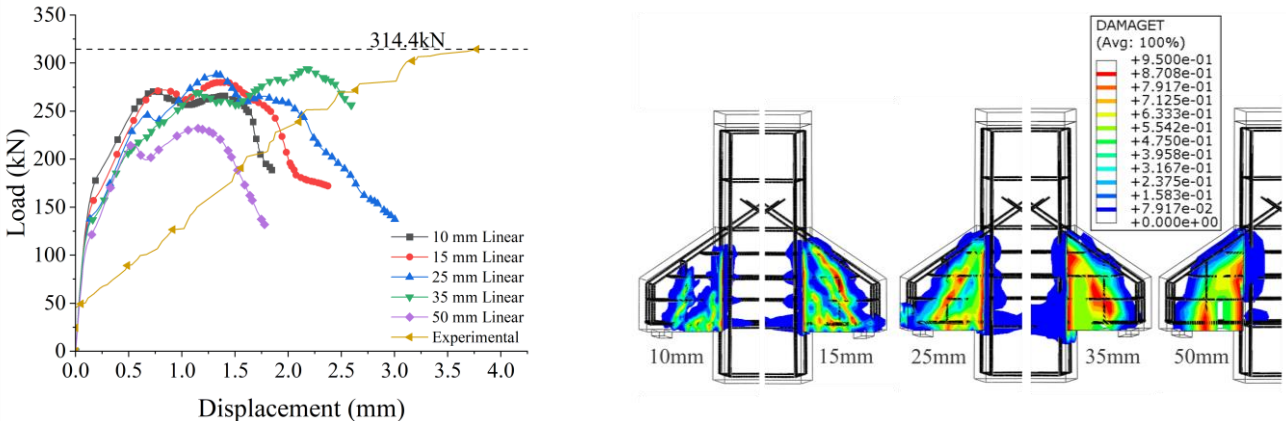

(**a**) (**b**)

Figure 5. Mesh refinement analysis: (**a**) Mesh analysis; (**b**) Tensile damage distribution in different mesh sizes.

Other authors also chose to use finite elements of the type C3D8R and T3D2 in their modeling, with an average mesh size varying between 20 and 50 mm [24,25,27,40–42]. This same mesh proportion with C3D8R and T3D2 elements will be used in the other models of this work. The proportion is calculated with the smallest dimension of the corbel and the size of the finite element, according to Equation (7) below.

$$T_s = \frac{M_s}{S_s} = \frac{25}{200} = 0.125 \quad (7)$$

where T_s is the mesh size ratio, M_s is the size of the chosen finite element (25 mm) and S_s is the smallest side among the three dimensions of the corbel. From this proportion, the mesh size can be calculated for the other specimens, which makes it possible to adjust the mesh size to the size of the corbel, respecting the refinement analysis carried out.

6. Sensitivity Analysis

In order to calibrate the CDP model used in corbels, a sensitivity analysis was performed. Two specific CDP parameters were analyzed, which are the deviatoric plane shape factor (K_c) and dilation angle (ψ). According to Lubliner et al. [22], the value of K_c can vary between 0.5 and 1.0. According to Behnam et al. [24], it is common for the dilation angle to vary between 30° and 42°. The shape factor was tested with four different values, and the expansion angle with five values, resulting in a total of 20 analyses. Figure 6 shows the schematic of the sensitivity analysis performed.

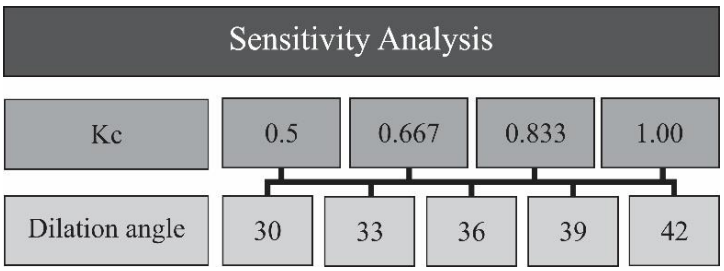

Figure 6. Sensitivity analysis values.

7. Sensitivity Analysis Results

7.1. Evaluation of the Dilation Angle (ψ) with Constant (Kc)

In this section, the influence of the expansion angle (ψ) was studied when the other CDP variables were constant. Figure 7 presents the results of the 20 analyses carried out. It is observed that the dilation angle has a great influence on the ultimate resistance achieved by the model and that there is a tendency for strength to increase when the value of the dilation angle increases.

In practice, the increase in corbel strength with increasing dilatancy angle occurs due to the influence of this variable on the tri-axial stress state of the concrete. Increasing the dilatancy angle increases the transverse deformations of the concrete in the strut region (similar to Poisson's ratio for the elastic regime), as can be seen in Figure 8. Due to the restriction of concrete deformations in the transverse direction of the strut due to the presence of seam reinforcement and the surrounding concrete itself, there is confinement of the strut for greater dilatancy angles, which increases the compressive strength of the concrete in this region and, consequently, corbels that break due to crushing of the concrete.

Figure 7b presents the best response among all the options analyzed, with a dilation angle of 39° and a Kc of 0.667, obtaining a ratio between numerical ultimate load ($V_{u,num}$) and experimental ultimate load ($V_{u,exp}$) of 1.003.

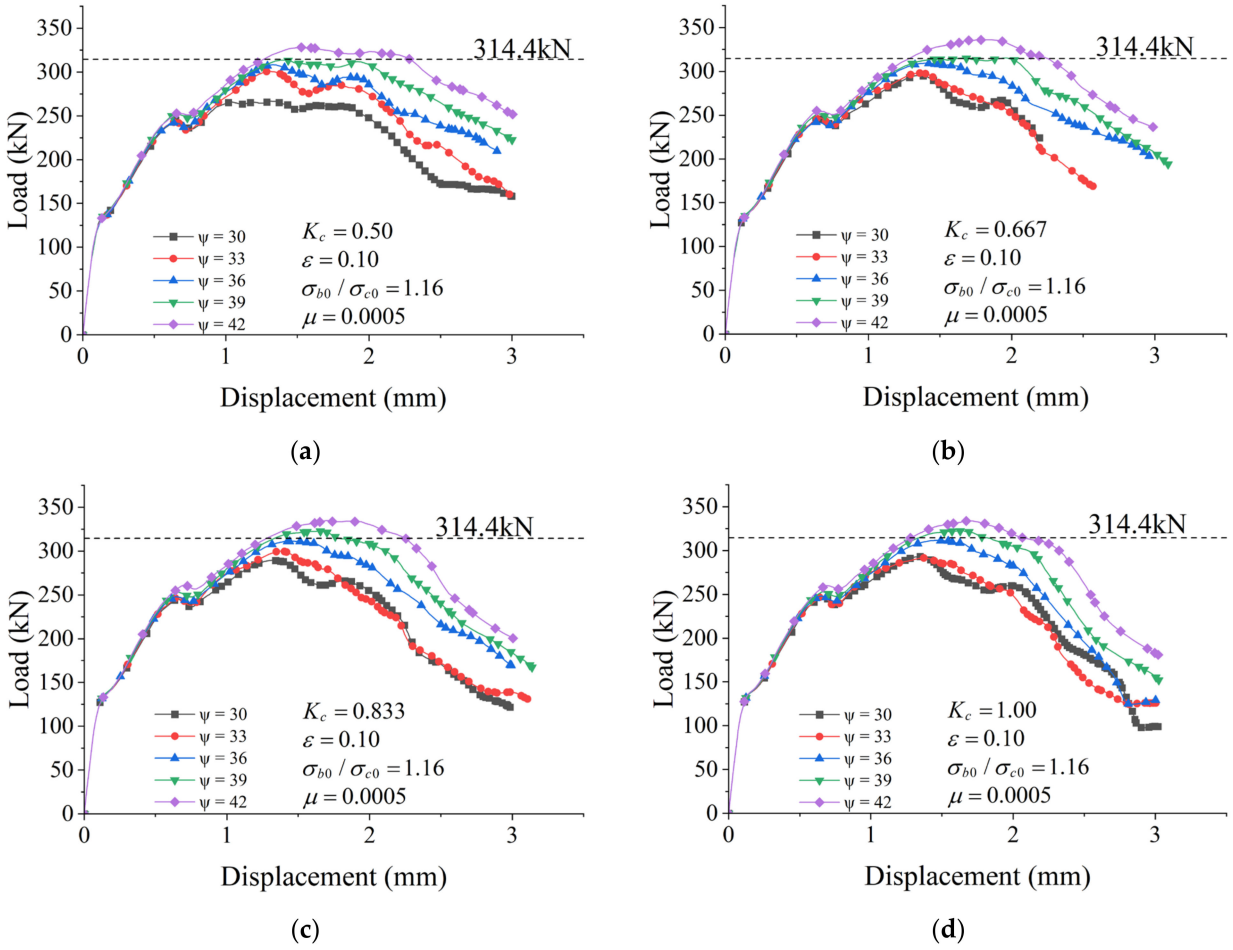

Figure 7. Sensitivity analysis with constant Kc and different dilation angles: (**a**) Sensitivity analysis with Kc = 0.50; (**b**) Sensitivity analysis with Kc = 0.667; (**c**) Sensitivity analysis with Kc = 0.833; (**d**) Sensitivity analysis with Kc = 1.00.

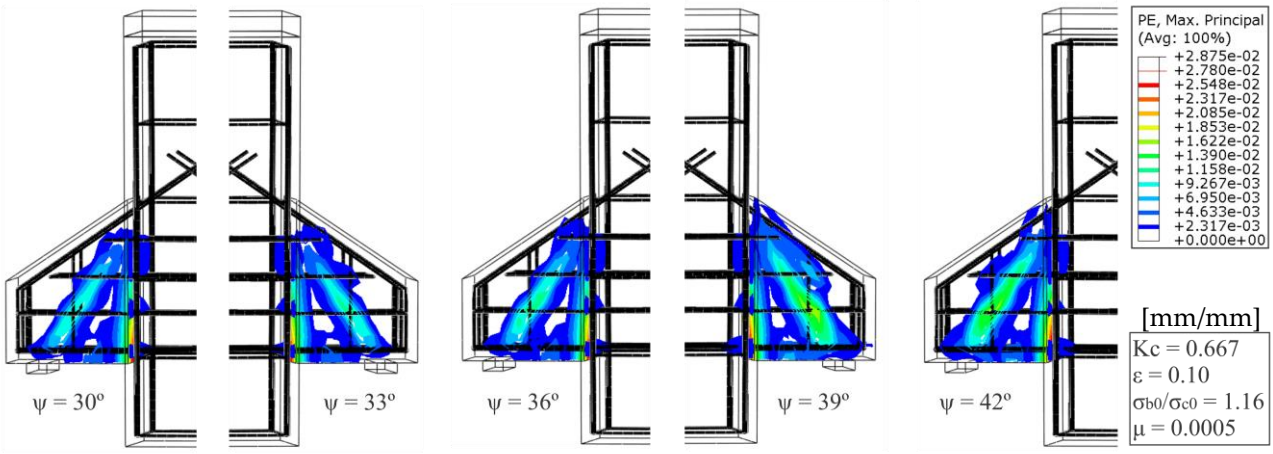

Figure 8. Tensile plastic deformations for different dilation angles.

7.2. Variation of Plane Shape Factor (Kc) with Constant Dilation Angle (ψ)

In this item, the influence of the deviatoric plane shape factor (K_c) is studied when the other CDP variables are constant. In Figure 9a,b, the results with dilation angles of 36° and 39°, respectively, are presented. What can be seen is that (K_c) has little influence on the behavior until failure, mainly affecting the post-peak section of the load × displacement curve.

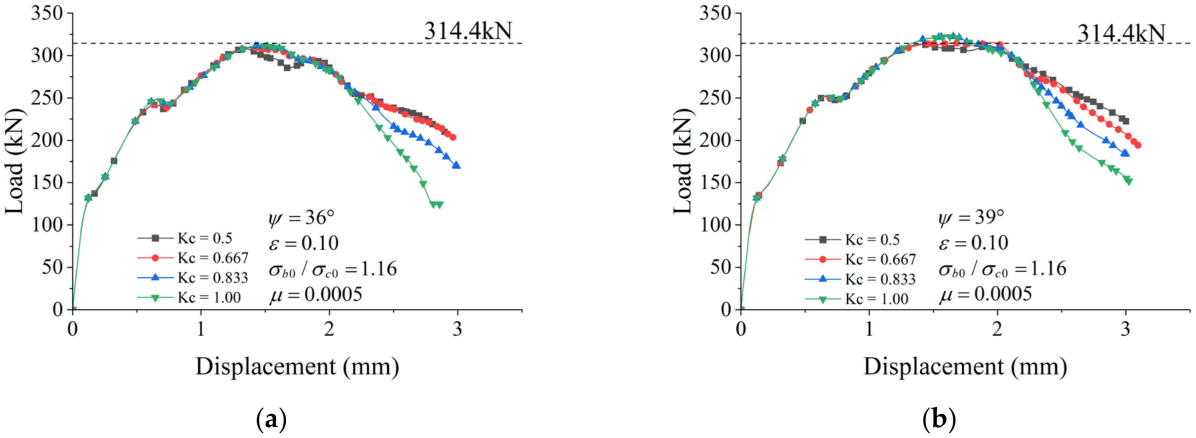

Figure 9. Sensitivity analysis with constant ψ and different K_c: (**a**) Sensitivity analysis with ψ = 36°; (**b**) Sensitivity analysis with ψ = 39°.

When comparing the two images, it is observed that the best correspondence to the results of the M3-MONO-A specimen is with a (Kc) of 0.667 and (ψ) of 39°. The value of 0.667 for Kc is recommended according to [43]. These same CDP values will be used in other corbels in order to understand whether such parameters can be standardized for corbels in general or whether an individualized study is necessary to calibrate the variables.

8. Evaluation of Numerical Results

This item demonstrates the results obtained from numerical modeling in comparison with experimental results with the aim of validating the proposed approach and demonstrating the efficiency of CDP in predicting results.

8.1. Modeling of the M3-MONO-A Corbel

The M3-MONO-A corbel was used in the sensitivity study already presented, and the best prediction regarding resistance occurred with an expansion angle ψ = 39° and coefficient Kc = 0.667. Using this model, experimental and numerical results will be compared in terms of load-bearing capacity, reinforcement deformation and cracking pattern.

Figure 10a,b show the deformation results of the tie rod reinforcement and the first layer of seam reinforcement, respectively. A good correlation was obtained between the experimental and numerical results, but it is worth highlighting that, in general, the numerical model is more rigid in the initial loading stages. One of the reasons for this is the consideration of perfect adhesion between the steel and the reinforcement (adopted for simplification) and possible accommodations in the test support system not considered in the numerical model. Figure 10b shows the results of the four strain gauges used to measure the deformation of the seam reinforcement, and it is observed that the numerical result corresponds well to the experimental results, except for the initial section, whose numerical model is more rigid.

Figure 11 shows the evolution of the main compression stresses with the evolution of the load. When 250 kN of load is applied to each corbel (Figure 11b), it is already possible to observe the formation of the compression strut and the stress concentration in the nodal region of the corbel support plate. Figure 11c shows the stress distribution when the maximum load was reached, and Figure 11d shows the post-peak stresses of the console when the loading capacity exceeded the maximum limit and the stresses were redistributed, generating a less uniform distribution of stresses. Comparing Figure 11c,d, it is possible to clearly observe the formation of a bottle-shaped connecting rod (with two compressed edges and one central core pulled in the direction perpendicular to the strut) due to tensile stresses transverse to the strut.

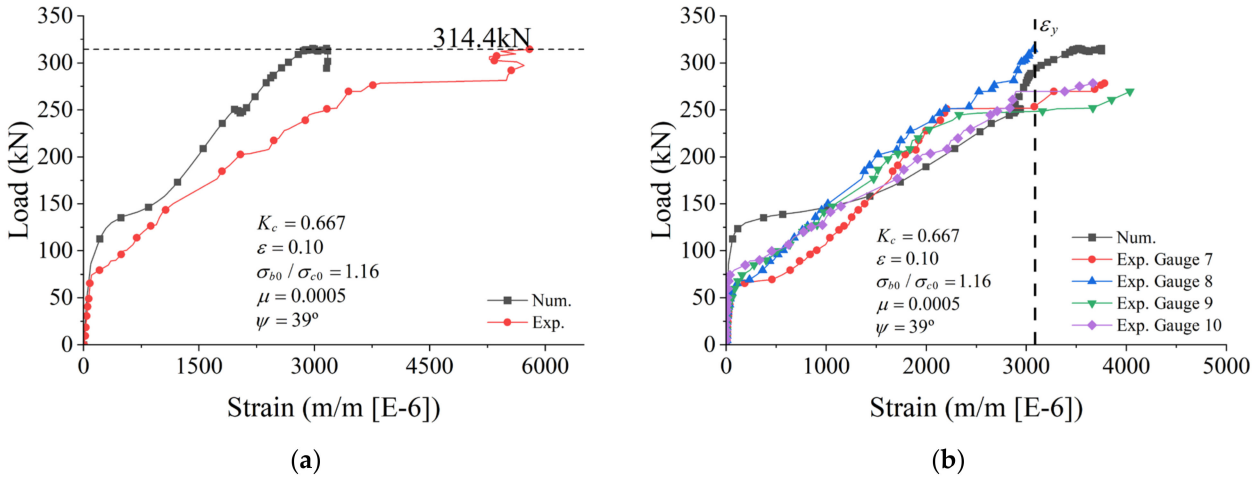

Figure 10. Force × strain in corbel reinforcement M3-MONO-A: (**a**) Tie reinforcement deformations; (**b**) Seam reinforcement deformation.

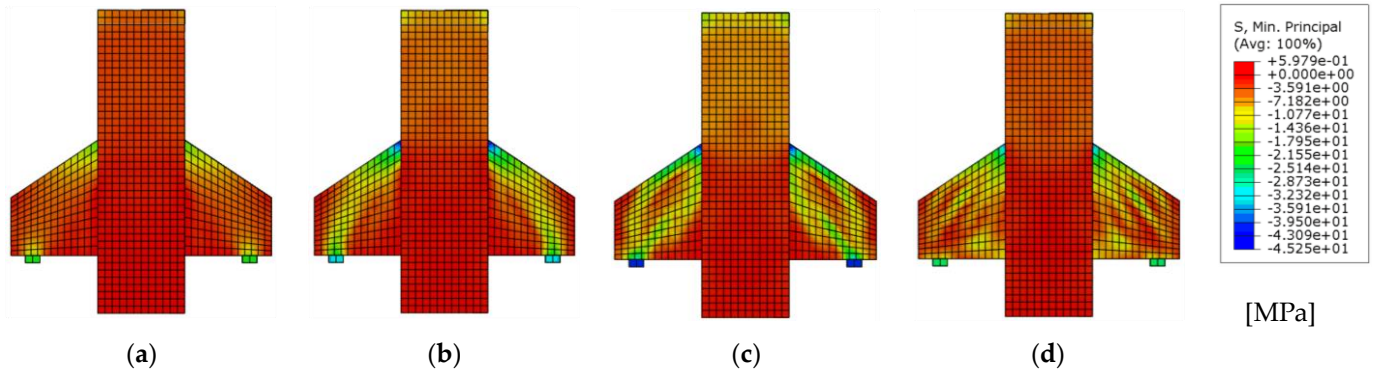

Figure 11. Numerical results of the evolution of the principal compressive stresses of the specimen M3-MONO-A: (**a**) M3-MONO-A-150kN; (**b**) M3-MONO-A-250kN; (**c**) M3-MONO-A-315kN peak; (**d**) M3-MONO-A-200kN post-peak.

Figures 12 and 13 show the evolution of tensile and compressive damage, respectively. Increased loads after reaching peak strength cause degradation in concrete. This degradation causes gradual loss of strength and is interpreted as tensile or compressive damage. Tensile damage (DAMAGET) can be interpreted as the formation of cracks as load increases, while compressive damage (DAMAGEC) relates to the crushing of concrete.

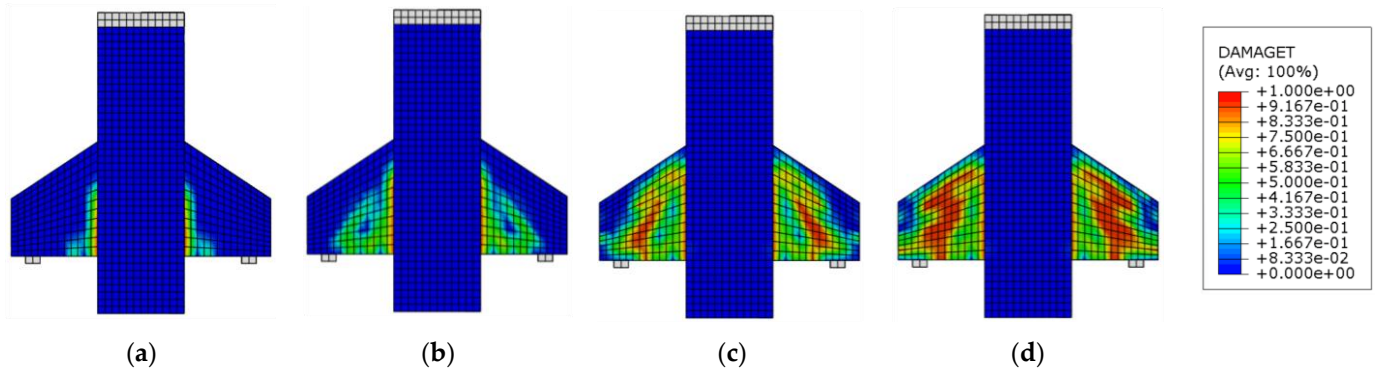

Figure 12. Numerical results of specimen tensile damage evolution M3-MONO-A: (**a**) M3-MONO-A-150kN; (**b**) M3-MONO-A-250kN; (**c**) M3-MONO-A-315kN peak; (**d**) M3-MONO-A-200kN post-peak.

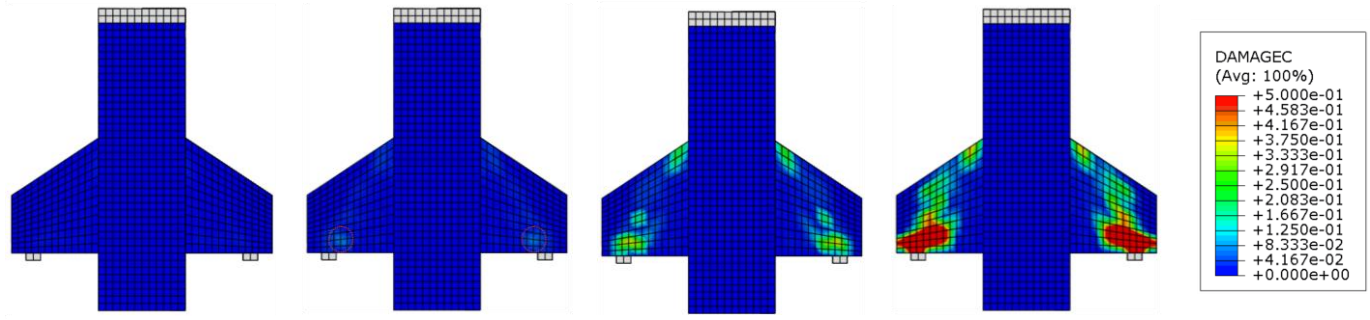

(**a**) (**b**) (**c**) (**d**)

Figure 13. Numerical results of the damage evolution under compression of the specimen. M3-MONO-A: (**a**) M3-MONO-A-150kN; (**b**) M3-MONO-A-250kN; (**c**) M3-MONO-A-315kN peak; (**d**) M3-MONO-A-200kN post-peak.

When comparing the damage results in Figures 12 and 13 with the experimental results in Figure 14, an excellent correspondence between the results is observed. The first crack appears at the corbel–column interface in the initial loading stage (Figure 12a). Then, inclined cracks appear in the strut region, and there is an increase in the crack at the interface (Figure 12b,c). Finally, the corbel breaks with the tie reinforcement yield (Figure 10a), the seam reinforcement yield (Figure 10b) and the crushing of the concrete in the nodal region (Figures 13c and 14b).

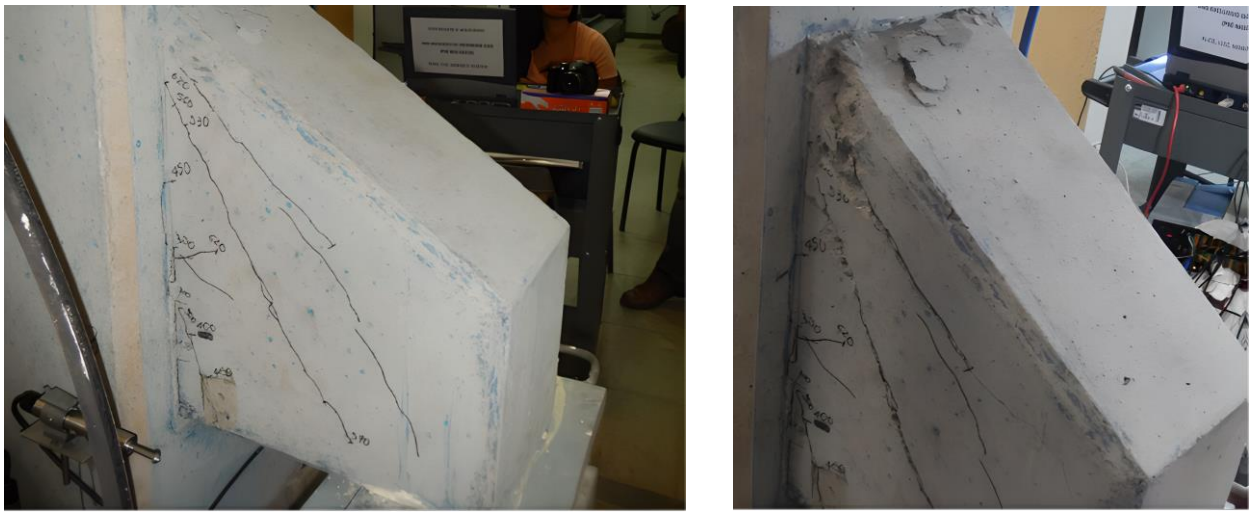

(**a**) (**b**)

Figure 14. Experimental results of specimen M3-MONO-A [10]: (**a**) Side view with opening cracks in the corbel; (**b**) Concrete crushing in the nodal region.

By comparing the numerical and experimental results, it could be stated that the modeling carried out with the Abaqus® software and CDP can predict the behavior and strength of the M3-MONO-A corbel.

8.2. Corbel FA-T8 Modeling

The same CDP parameters were tested on FA-T8 and FE-SC6-4A corbels to investigate whether it is possible to generalize the chosen parameters to other corbels with different geometry, concrete properties and reinforcement ratios. Figure 15 shows the results of the load × displacement curve with the CDP parameters used in the M3-MONO-A specimen. The relationship between numerical load/experimental load was 0.778, i.e., the resistance obtained was 22% lower than that achieved experimentally.

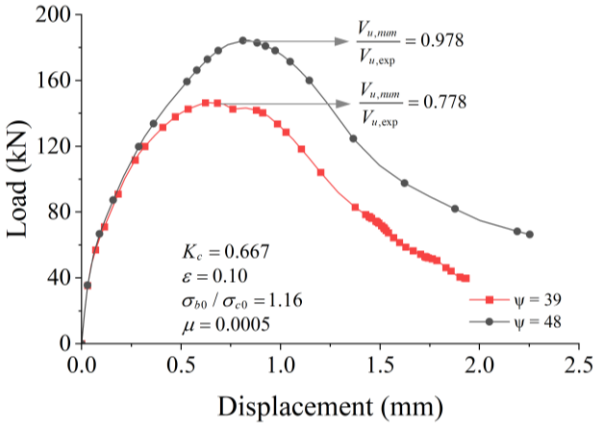

Figure 15. Numeric results for force × displacement curve with proposed dilation angle.

A new sensitivity analysis was performed by modifying the dilation angle (ψ), and the best result occurred with 48° of dilation, as can be seen in Figure 14, with $V_{u,num}/V_{u,exp}$ = 0.978 and an error of 2.2%.

In addition to strength, the deformation values of the tie and seam reinforcement, the distribution of the main compressive stresses, and the tensile and compressive damage were obtained and compared, as shown in Figures 16–19, respectively. The reinforcement strain results obtained a good correspondence when compared with the experimental results, with the numerical model being stiffer again in the initial loading stages Figure 16a.

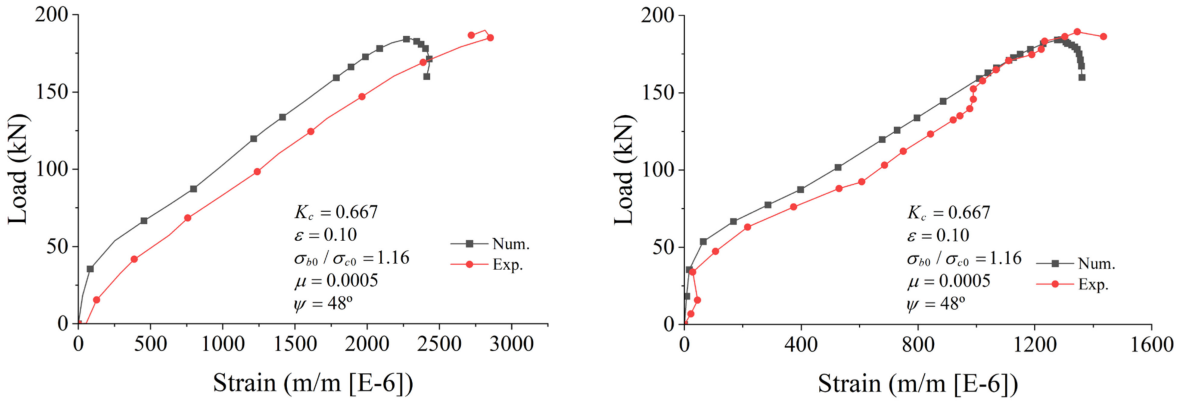

Figure 16. Force × strain on corbel reinforcement FA-T8: (**a**) Strain on tie reinforcement; (**b**) Strain in seam reinforcement.

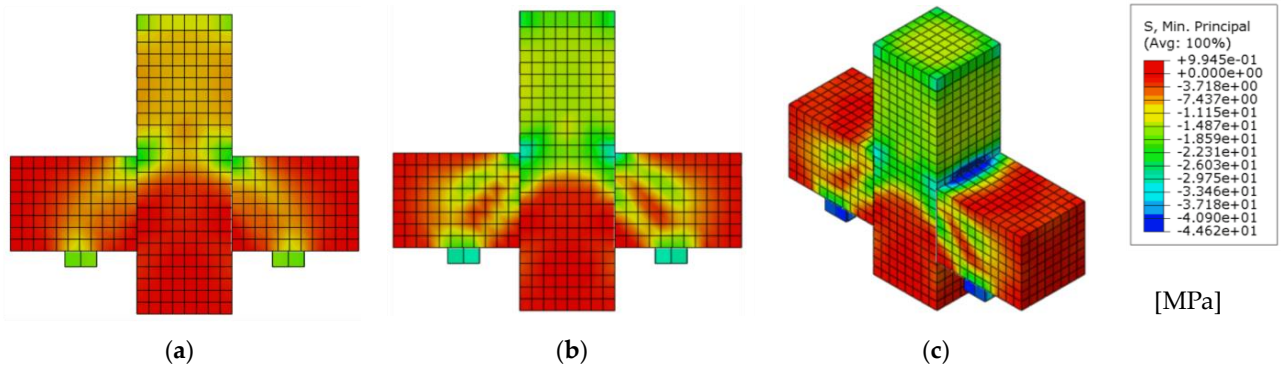

Figure 17. Numerical results of the evolution of the principal compressive stresses of the specimen FA-T8: (**a**) FA-T8-100kN; (**b**) FA-T8-160kN; (**c**) FA-T8-185kN peak.

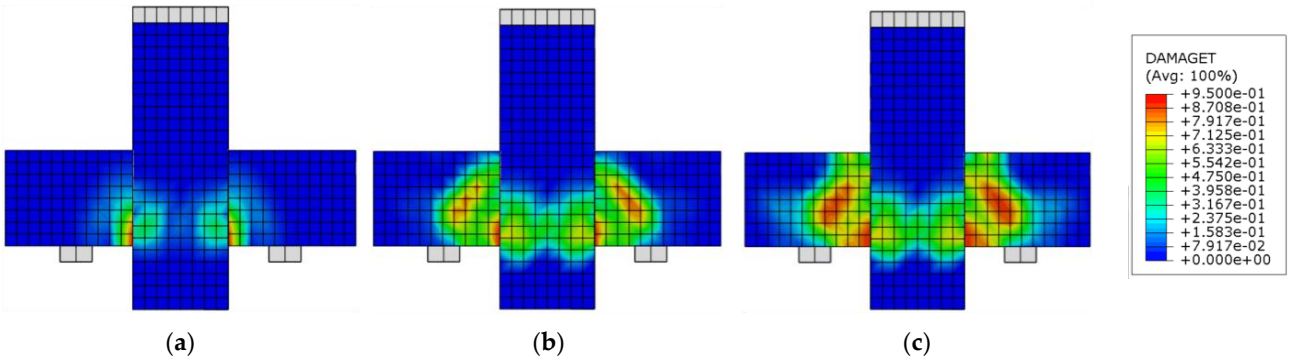

Figure 18. Numerical results of specimen tensile damage evolution FA-T8: (**a**) FA-T8-100kN; (**b**) FA-T8-185kN peak; (**c**) FA-T8-100kN post-peak.

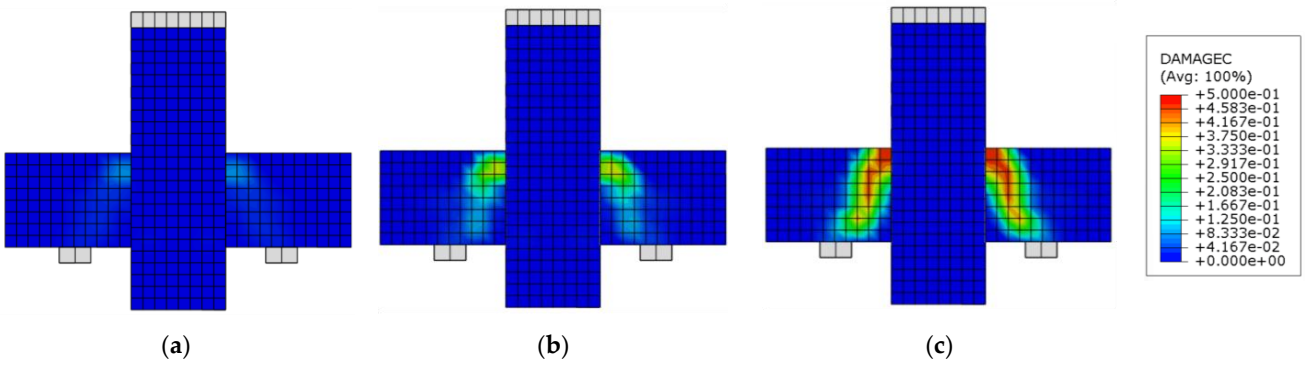

Figure 19. Numerical results of specimen compressive damage evolution FA-T8: (**a**) FA-T8-100kN; (**b**) FA-T8-185kN peak; (**c**) FA-T8-100kN post-peak.

Figure 20 shows the distribution of cracks and the mode of failure of the experimentally tested FA-T8 corbel. The collapse occurred due to the yielding of the tie reinforcement, followed by the crushing of the concrete in the nodal region. The first cracks appear at the corbel–column interface, and as the load increases, diagonal cracks appear parallel to the compression strut. Finally, when the corbel reaches its maximum load capacity, the tie reaches yield, allowing a greater opening of the crack at the interface and a relative rotation between the corbel and the column, which causes the concrete to crush in the nodal region, as can be seen in Figure 20.

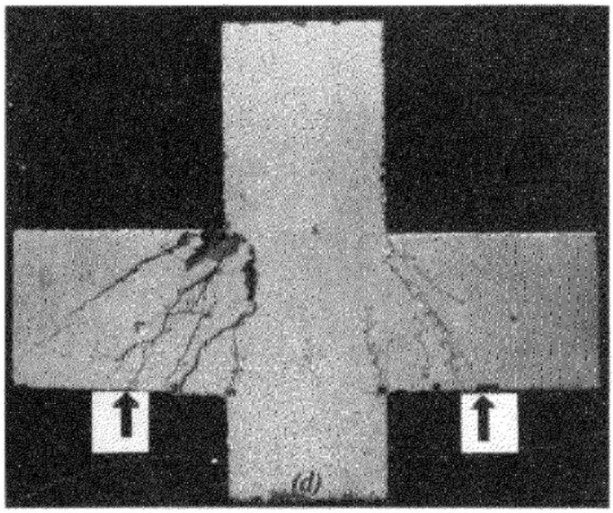

Figure 20. Experimental results of the specimen FA-T8 [11].

When comparing the experimental results with the concrete damage to tension and compression (Figures 18 and 19, respectively), it is observed that the numerical failure mode was the same as the experimental one, with tensile damage at the interface and inclined parallel to the strut, and compression damage generated by the crushing of concrete in the nodal region.

8.3. Corbel FE-CS6-4A Modeling

The results for the FE-CS6-4A corbel were similar to the FA-T8 specimen shown above. When testing the expansion angle of 39°, the results were conservative, as can be seen in Figure 21a, showing a relationship $V_{u,num}/V_{u,exp}$ = 0.917, which represents an error of 8.1%. The sensitivity analysis of the dilation angle obtained the ideal value of 51°, with $V_{u,num}/V_{u,exp}$ = 1.019, and an error of only 1.9%. Figure 21b shows the yield results of the tie reinforcement when compared with the experimental results.

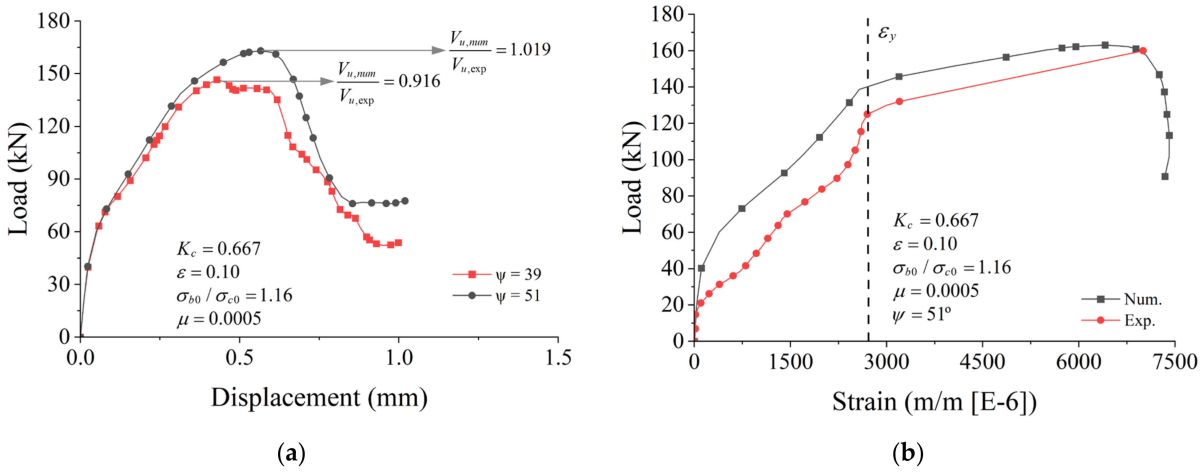

Figure 21. Numerical modeling of corbel FE-CS6-4A: (**a**) Load × displacement with proposed angle; (**b**) Load × strain in tie reinforcement.

The author who tested the corbel FE-SC6-4A [11] did not make images of the corbel's ruin available in his study, yet in Figures 22–24, the numerical results of main compressive stress, tensile damage and compressive damage are presented, respectively.

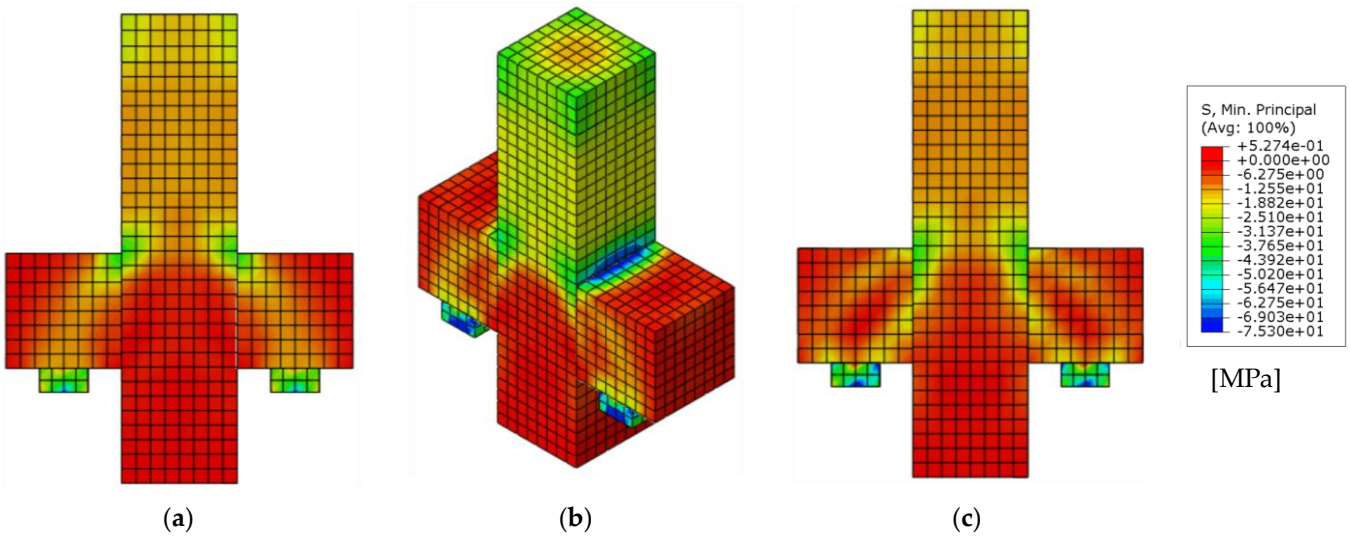

Figure 22. Numerical results of compression principal stress evolution of specimen FE CS6-4A: (**a**) FE-SC6-4A-100kN; (**b**) FE-SC6-4A-162kN peak; (**c**) FE-SC6-4A-90kN post-peak.

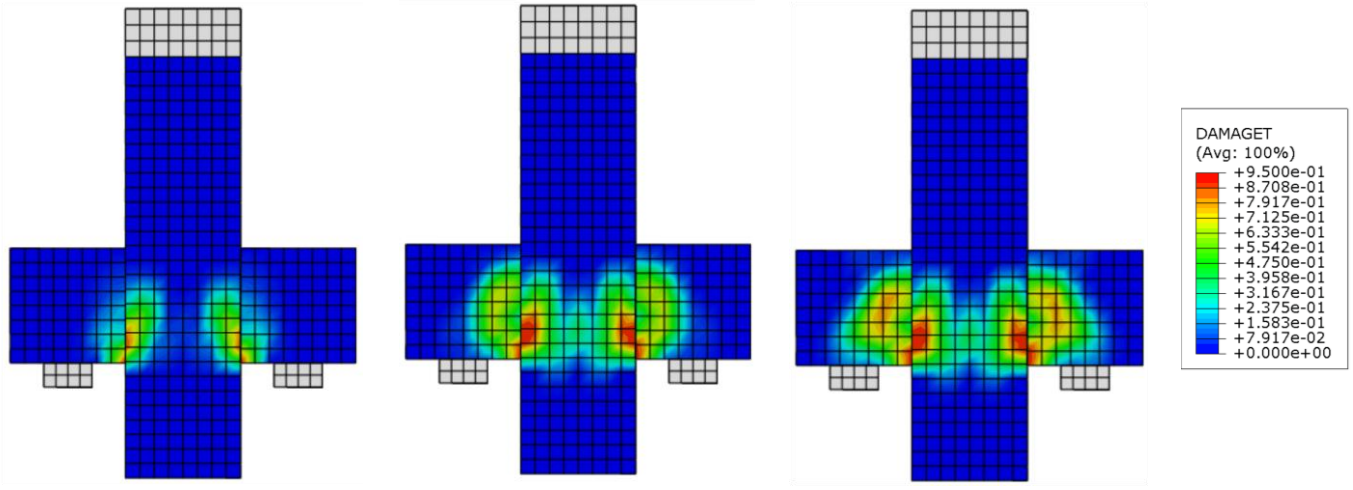

Figure 23. Numerical results of specimen tensile damage evolution FE SC6-4A: (**a**) FE-SC6-4A-100kN; (**b**) FE-SC6-4A-162kN PICO; (**c**) FE-SC6-4A-90kN PÓS-PICO.

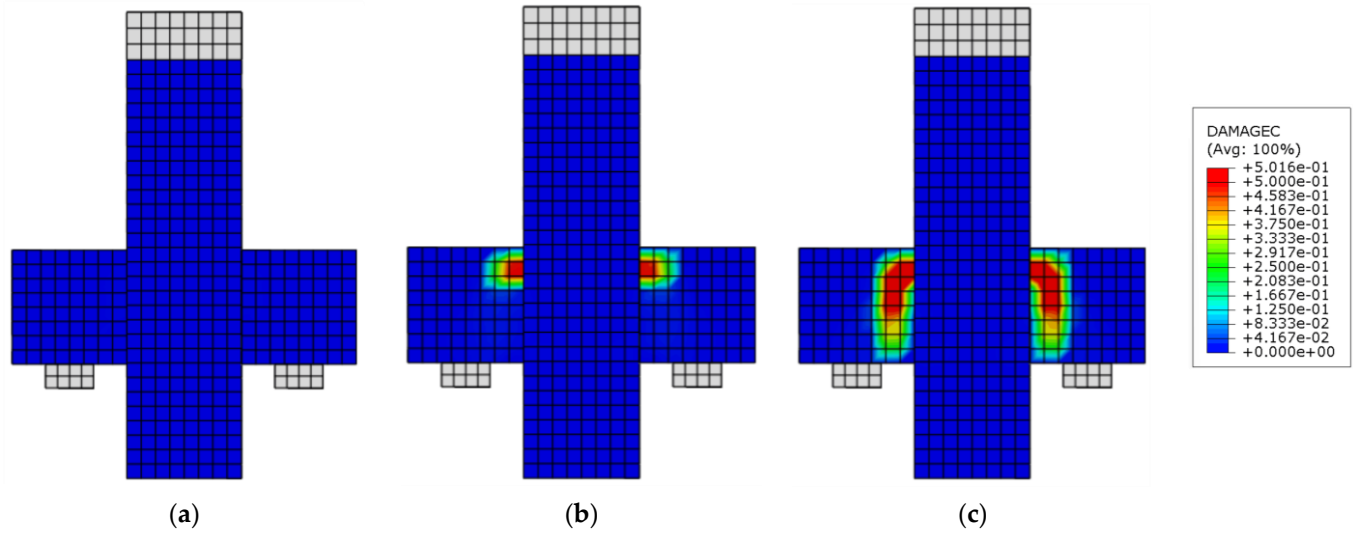

Figure 24. Numerical results of specimen compressive damage evolution FE SC6-4A: (**a**) FE-SC6-4A-100kN; (**b**) FE-SC6-4A-162kN peak; (**c**) FE-SC6-4A-90kN post-peak.

The results indicate that the failure mode was initially caused by the opening of a crack at the interface (Figure 23a), followed by the crushing of the concrete in the nodal region after reinforcement yielding (Figure 24b). The post-peak behavior indicates a large compression damage located in the strut region Figure 24c.

As with the M3-MONO-A and FA-T8 corbels, the FE-CS6-4A specimen was numerically modeled and obtained good results using Abaqus® software and CDP.

9. Comparison of Calibrations with Different Dilatancy Angles

Table 4 presents the level of precision achieved by the $V_{u,num}/V_{u,exp}$ relationship using different dilatancy angle values: 39°, 48° and 51°. The average value of $V_{u,num}/V_{u,exp}$ varied from 0.90 with ψ = 39° to 1.09 with ψ = 51°. The coefficient of variation reduced from 12.63% to 8.42% by increasing ψ from 39° to 51°. Therefore, it may be stated that the average error in corbel strength predictions ranged around 10% in variations on the dilation angle. When analyzing the results of $V_{u,num}/V_{u,exp}$ separately for each test, it is observed

that the maximum error in corbel strength predictions reached 22% for the FA-T8 test and ψ = 39°. The $V_{u,num}/V_{u,exp}$ ratio closest to unity, on average, was reached with ψ = 48°.

Table 4. Comparison of numerical results with fixed dilation angle.

Experimental		**Numerical ψ = 39°**		**Numerical ψ = 48°**		**Numerical ψ = 51°**	
Corbel	$V_{u,exp}$	$V_{u,num}$	$\frac{V_{u,num}}{V_{u,exp}}$	$V_{u,\ num}$	$\frac{V_{u,num}}{V_{u,exp}}$	$V_{u,num}$	$\frac{V_{u,num}}{V_{u,exp}}$
M3-MONO-A	314.42	315.32 *	1.00 *	367.65	1.17	374.99	1.19
FA-T8	188.40	146.53	0.78	184.35 *	0.98 *	198.63	1.05
FE SC6-4A	160.00	146.60	0.92	154.74	0.97	163.07 *	1.02 *
Mean value		0.90		1.04		1.09	
Standard deviation		0.114		0.114		0.092	
COV (%)		12.63		10.94		8.42	

* Indicates the best adjustment of the dilatancy angle with the studied console.

The results highlighted in Table 4 indicate the best adjustment of the dilation angle for each corbel and, in turn, that it may not be possible to generalize a single set of CDP parameters to represent all concrete classes, but rather that each specimen must have the CDP parameters studied and calibrated individually according to the class of concrete used since dilatancy is a property of the material. Furthermore, it is important to highlight that ABAQUS® uses a constant dilatancy value throughout the simulation. Still, it is known that the dilatancy value varies depending on the level of stress and strain of the concrete [35]. In practice, the dilatancy of the material reduces as the plastic deformations of the concrete increase. For this reason, it is natural that the optimum dilatancy angle for each corbel varies since each corbel fails at a different level of stress and deformation in the strut. When using the optimal dilatancy values for each corbel, $V_{u,num}/V_{u,exp}$ = 1.00, and a coefficient of variation of just 2% were obtained.

10. Analytical Models Comparison

In this item, analytical results of compression strut strength are obtained using the strut and tie models of ABNT NBR 9062:2017 [1], PCI [2] and EN 1992-1-1:2004 [3]. The deduction of the equations used is available in the study by Araújo et al. [14]. As one of the purposes is to evaluate the ability of the analytical models to predict the real strength of the corbel, no safety coefficient will be used, and mean values of material properties were considered instead of characteristic values.

Table 5 presents the results obtained for the three analytical models, in addition to the numerical results of this study. The PCI model was the one that came closest to the experimental results, with an average analytical ultimate load/experimental ultimate load of 1.62 ($V_{u,ana}/V_{u,exp}$ = 1.62), which represents an average error of 62%. In general, all analytical models overestimate the corbel strength and present a high coefficient of variation, between 26.73% and 40.52%, which is in line with the results found by Araújo et al. [14].

Table 5. Comparison between experimental, numerical and analytical results.

Experimental		**Numerical ψ = 48°**		**NBR 9062**		**PCI**		**EN 1992-1-1**	
Corbel	$V_{u,exp}$	$V_{u,num}$	$V_{u,num}/V_{u,exp}$	$V_{u,ana}$	$V_{u,ana}/V_{u,exp}$	$V_{u,ana}$	$V_{u,ana}/V_{u,exp}$	$V_{u,ana}$	$V_{u,ana}/V_{u,exp}$
M3-MONO-A	314.42	367.65	1.17	421.98	1.34	735.5	2.34	691.52	2.20
FA-T8	188.40	184.35	0.98	395.9	2.10	200.6	1.06	181.60	0.96
FE CS6-4A	160.00	154.74	0.97	371.3	2.32	230.8	1.44	290.90	1.82
Mean values		1.04		1.92		1.62		1.66	
Standard deviation		0.114		0.514		0.655		0.633	
COV (%)		10.94		26.73		40.52		38.10	

When comparing the numerical and analytical results, it is possible to highlight the potential of the numerical model in predicting the results, as an average numerical ultimate load/experimental ultimate load of 1.04 was obtained ($V_{u,num}/V_{u,exp}$ = 1.04) and coefficient variation of only 10.94% when using a dilatancy of 48°. However, these results are linked to the calibration of the computational model and a good use of the constitutive models of the materials.

In general, the large differences in the accuracy level between the numerical models and the analytical expressions can be related to the following factors: (i) the analytical expressions all assume reinforcement yielding at failure; therefore, the level of accuracy tends to deviate more when the corbels fail by strut crushing or some nodal failure; (ii) the analytical expressions do not consider possible enhancements in the corbel capacity due to the contribution of secondary reinforcement acting as auxiliary ties; and (iii) the numerical models naturally allows considering any failure mechanism (at the strut, tie or nodal zone) straightforwardly as both concrete and reinforcements are modeled. Based on this explanation, it sounds natural that the numerical models, after proper calibration, stand out regarding the predictions of ultimate capacity. Despite some simplifications in the modeling, such as the perfect bond between reinforcement and concrete and homogeneous material properties along the corbels, the numerical models allow consideration of more parameters related to corbel behavior, such as the concrete and reinforcement non-linear behavior, for instance.

11. Conclusions

This study investigates the level of accuracy of different modeling choices to predict the ultimate capacity of reinforced concrete corbels using the concrete damage plasticity model. In addition, the ultimate capacity of the studied corbels was also predicted using current design code expressions. From the presented analyses and results, the following conclusions can be drawn:

In general, the analytical models of ABNT NBR 9062:2017, PCI, and EN 1992-1-1:2004 overestimate the corbel capacity and show a high coefficient of variation, with a relationship between analytical ultimate load and experimental ultimate load between 1.62 and 1.92 and a coefficient of variation between 26.7% and 40.5%.

The numerical model studies showed significantly better predictions of ultimate capacity than the investigated analytical models. Calibrating specifical parameters from the CDP for each test result, the average ratio between tested and predicted resistances reached 1.0, with a coefficient of variation of only 2.05%. Nevertheless, we also showed that using a fixed modeling choice regarding all CDP parameters, it is possible to reach an average ratio between tested and predicted resistances of 1.04, with a coefficient of variation of only 10.9%. As a general recommendation, the 48° dilatancy angle can be used in the absence of specific studies for normal and high-strength concrete in corbels. In addition, the following material parameters can be used in the modeling of RC corbels: (i) shape factor K_c = 0.667; eccentricity e = 0.1; viscosity μ = 0.0005; the ratio between biaxial and uniaxial compressive yield strength σ_{b0}/σ_{c0} = 1.16. The non-linear compressive and tensile behavior of concrete can be well represented with the models from Carreiran and Chu [37] and Peterson [44] (adapted by Genikomsou and Polak [29]), respectively. These things considered, the following simplifications can be assumed in the modeling: (i) perfect bond between reinforcement and concrete when anchorage failure is not critical; (ii) truss elements to model the reinforcement (T3D2); and (iii) solid elements with linear order integration to represent the concrete (C3D8R).

Author Contributions: Conceptualization, Y.M.N., M.V.A., A.M.D.d.S., M.B., E.P.d.S.J., H.F.d.S., B.C., E.A.B., V.B.d.M.A., A.L.C. and M.d.A.F.; methodology, Y.M.N., M.V.A., A.M.D.d.S. and A.L.C.; software, Y.M.N. and M.V.A.; validation, Y.M.N., M.V.A., A.M.D.d.S., M.B., H.F.d.S., B.C., E.A.B., V.B.d.M.A., A.L.C. and M.d.A.F.; formal analysis, Y.M.N., M.V.A., A.M.D.d.S., M.B., E.P.d.S.J., H.F.d.S., B.C., E.A.B., V.B.d.M.A., A.L.C. and M.d.A.F.; investigation, Y.M.N., M.V.A., A.M.D.d.S., M.B., H.F.d.S., B.C., E.A.B., V.B.d.M.A., A.L.C. and M.d.A.F.; resources, Y.M.N., M.V.A. and A.M.D.d.S.;

data curation, Y.M.N., M.V.A., A.M.D.d.S., M.B., H.F.d.S., B.C., E.A.B., V.B.d.M.A., A.L.C. and M.d.A.F.; writing—original draft preparation, Y.M.N., A.M.D.d.S., M.B., E.P.d.S.J., H.F.d.S., E.A.B. and V.B.d.M.A.; writing—review and editing, Y.M.N., M.V.A., A.M.D.d.S., M.B., E.A.B., V.B.d.M.A. and A.L.C.; visualization, Y.M.N., M.V.A., A.M.D.d.S., M.B., H.F.d.S., B.C., E.A.B., V.B.d.M.A., A.L.C. and M.d.A.F.; supervision, A.L.C. and M.d.A.F.; project administration, A.L.C. and M.d.A.F.; funding acquisition, Y.M.N., M.V.A., A.M.D.d.S., M.B., E.P.d.S.J., H.F.d.S. and A.L.C. All authors have read and agreed to the published version of the manuscript.

Funding: This study was financed by the Coordenação de Aperfeiçoamento de Pessoal de Nível Superior, Brasil (CAPES), finance code 001; by the Pró-Reitoria de Pesquisa, Inovação e Pós-Graduação of Instituto Federal de Rondônia (PROPESP/IFRO), finance code 002; and São Paulo Research Foundation (FAPESP, grant number #2021/13916-0).

Data Availability Statement: The data presented in this study are available on request from the corresponding author.

Acknowledgments: We would like to acknowledge the Pró-Reitoria de Pesquisa, Inovação e PósGraduação of Instituto Federal de Rondônia (PROPESP/IFRO), the Coordenação de Aperfeiçoamento de Pessoal de Nível Superior, Brazil (CAPES), and the São Paulo Research Foundation (FAPESP).

Conflicts of Interest: The authors declare no conflict of interest.

References

1. *ABNT NBR 9062*; Projeto e Execução de Estruturas de Concreto Pré-Moldado. Associação Brasileira de Normas Técnicas—ABNT: Rio de Janeiro, Brazil, 2017.
2. PCI. *PCI Design Handbook*, 7th ed.; PCI—Precast/Prestressed Concrete Institute: Chicago, IL, USA, 2010.
3. *EN 1992-1-1*; Eurocode 2: Design of Concrete Structures—Part 1-1: General Rules and Rules for Buildings. CEN—Comité Européen de Normalisation: Brussels, Belgium, 2004.
4. Foster, S.J.; Powell, R.E.; Selim, H.S. Performance of High-Strength Concrete Corbels. *ACI Struct. J.* **1996**, *93*, 555–563. [CrossRef]
5. Campione, G.; La Mendola, L.; Papia, M. Flexural Behaviour of Concrete Corbels Containing Steel Fibers or Wrapped with FRP Sheets. *Mater. Struct. Constr.* **2005**, *38*, 617–625. [CrossRef]
6. Campione, G.; La Mendola, L.; Mangiavillano, M.L. Steel Fiber-Reinforced Concrete Corbels: Experimental Behavior and Shear Strength Prediction. *ACI Struct. J.* **2007**, *104*, 570–579. [CrossRef]
7. Campione, G. Flexural Response of FRC Corbels. *Cem. Concr. Compos.* **2009**, *31*, 204–210. [CrossRef]
8. Yong, Y.-K.; Balaguru, P. Behavior of Reinforced High-Strength-Concrete Corbels. *J. Struct. Eng* **1994**, *120*, 1182–1201. [CrossRef]
9. Fernandes, G.B. Behavior of Reinforced High-Strength Concrete Corbels-Experimental Investigation and Design Model. *Am. Concr. Inst. ACI Spec. Publ.* **1999**, *SP186*, 445–462. [CrossRef]
10. Araújo, D.D.L.; Oliveira, E.M.D.; Silva, E.M.O.; Coelho, S.A.; El Debs, M.K. Experimental Analysis of a Modified Two-Step Corbel for Precast Concrete System. *Eng. Struct.* **2021**, *242*, 112585. [CrossRef]
11. Fattuhi, N.I.; Hughes, B.P. Ductility of Reinforced Concrete Corbels Containing Either Steel Fibers or Stirrups. *Struct. J.* **1989**, *8*, 644–651.
12. Fattuhi, N.I. Column-Load Effect on Reinforced Concrete Corbels. *J. Struct. Eng.* **1990**, *116*, 188–197. [CrossRef]
13. Fattuhi, N.I. Reinforced Corbels Made with High-Strength Concrete and Various Secondary Reinforcements. *ACI Struct. J.* **1994**, *91*, 376–383. [CrossRef]
14. Araújo, D.L.; Silva Neto, A.P.; Lobo, F.A.; El Debs, M.K. Comparative Analysis of Design Models for Concrete Corbels. *Rev. IBRACON Estrut. Mater.* **2016**, *9*, 435–470. [CrossRef]
15. Michał, S.; Andrzej, W. Analysis of "d" Regions of RC Structures Based on Example of Frame Corners. *AIP Conf. Proc.* **2018**, *1922*, 130002. [CrossRef]
16. Beshara, F.B.A.; Mustafa, T.S.; Mahmoud, A.A.; Khalil, M.M.A. Constitutive Models for Nonlinear Analysis of SFRC Corbels. *J. Build. Eng.* **2020**, *28*, 101092. [CrossRef]
17. Syroka, E.; Bobiński, J.; Tejchman, J. FE Analysis of Reinforced Concrete Corbels with Enhanced Continuum Models. *Finite Elem. Anal. Des.* **2011**, *47*, 1066–1078. [CrossRef]
18. Canha, R.M.F.; Kuchma, D.A.; El Debs, M.K.; Souza, R.A. de Numerical Analysis of Reinforced High Strength Concrete Corbels. *Eng. Struct.* **2014**, *74*, 130–144. [CrossRef]
19. Araújo, D.D.L.; Coelho, S.A.; Almeida, S.R.M.; El Debs, M.K. Computational Modelling and Analytical Model for Two-Step Corbel for Precast Concrete System. *Eng. Struct.* **2021**, *244*, 112699. [CrossRef]
20. Neuberger, Y.M.; de Lima Araújo, D. An Improved Analytical Model for Two-Step Corbels in a Precast Concrete System. *Eng. Struct.* **2023**, *284*, 115947. [CrossRef]
21. *Simulia Abaqus 6.11 Theory Manual*; Dassault Systèmes Simulia Corp.: Providence, RI, USA, 2017; Volume IV, p. 1172.
22. Lubliner, J.; Oliver, J.; Oller, S.; Oñate, E. A Plastic-Damage Model for Concrete. *Int. J. Solids Struct.* **1989**, *25*, 299–326. [CrossRef]
23. Jeeho, L.; Gregory, L.F. Plastic-Damage Model for Cyclic Loading of Concrete Structures. *J. Eng. Mech.* **1998**, *124*, 892–900.

24. Behnam, H.; Kuang, J.S.; Samali, B. Parametric Finite Element Analysis of RC Wide Beam-Column Connections. *Comput. Struct.* **2018**, *205*, 28–44. [CrossRef]
25. Panahi, H.; Genikomsou, A.S. Comparative Evaluation of Concrete Constitutive Models in Non-Linear Finite Element Simulations of Slabs with Different Flexural Reinforcement Ratios. *Eng. Struct.* **2022**, *252*, 113617. [CrossRef]
26. Chen, R.P.; Ma, Q.L.; Zhang, Y.; Wu, H.N.; Liu, Y.; Lu, L. Experimental Study on the Mechanical Behaviour of Eccentric Compression Short Column Strengthened by Ultra-High-Performance Fibre-Reinforced Concrete. *Structures* **2021**, *33*, 508–522. [CrossRef]
27. Hany, N.F.; Hantouche, E.G.; Harajli, M.H. Finite Element Modeling of FRP-Confined Concrete Using Modified Concrete Damaged Plasticity. *Eng. Struct.* **2016**, *125*, 1–14. [CrossRef]
28. Zhao, W.S.; Chen, W.Z. Effect of Near-Fault Ground Motions with Long-Period Pulses on the Tunnel. *J. Vibroeng.* **2015**, *17*, 841–858.
29. Genikomsou, A.S.; Polak, M.A. Finite Element Analysis of Punching Shear of Concrete Slabs Using Damaged Plasticity Model in ABAQUS. *Eng. Struct.* **2015**, *98*, 38–48. [CrossRef]
30. Reginato, L.; de Sousa, A.M.D.; Santos, J.V.C.; El Debs, M.K. NLFEA of Reinforced Concrete Corbels: Proposed Framework, Sensibility Study, and Precision Level. *Buildings* **2023**, *13*, 1874. [CrossRef]
31. de Sousa, A.M.D.; Lantsoght, E.O.L.; Genikomsou, A.S.; Prado, L.P.; El Debs, M.K. NLFEA of One-Way Slabs in Transition between Shear and Punching: Recommendations for Modeling. *Eng. Struct.* **2023**, *293*, 116617. [CrossRef]
32. Hegemier, G.A.; Nunn, R.O.; Arya, S.K. Behavior of Concrete Masonry Under Biaxial Stresses. In Proceedings of the North American Masonry Conference, Denver, CO, USA, 14–16 August 1978; pp. 656–666.
33. Kupfer, H.B.; Hilsdorf, H.K.; Rusch, H. Behavior of Concrete Under Biaxial Stresses. *ACI J. Proc.* **1969**, *66*, 656–666. [CrossRef]
34. Kupfer, H.B.; Gerstle, K.H. Behavior of Concrete under Biaxial Stresses. *J. Eng. Mech. Div.* **1973**, *99*, 853–866. [CrossRef]
35. Poliotti, M.; Bairán, J.M. A New Concrete Plastic-Damage Model with an Evolutive Dilatancy Parameter. *Eng. Struct.* **2019**, *189*, 541–549. [CrossRef]
36. Cheng, H.; Paz, C.M.; Pinheiro, B.C.; Estefen, S.F. Experimentally Based Parameters Applied to Concrete Damage Plasticity Model for Strain Hardening Cementitious Composite in Sandwich Pipes. *Mater. Struct. Constr.* **2020**, *53*, 78. [CrossRef]
37. Carreira, D.J.; Chu, K.H. Stress-Strain Relatonship for Reinforced Concrete in Compression. *ACI Struct. J.* **1985**, *83*, 21–28.
38. Yu, T.; Teng, J.G.; Wong, Y.L.; Dong, S.L. Finite Element Modeling of Confined Concrete-II: Plastic-Damage Model. *Eng. Struct.* **2010**, *32*, 680–691. [CrossRef]
39. Comité Euro-International du Béton. *CEB-FIB-Model Code 1990: Design Code*; Thomas Telford: London, UK, 1993.
40. Chi, Y.; Yu, M.; Huang, L.; Xu, L. Finite Element Modeling of Steel-Polypropylene Hybrid Fiber Reinforced Concrete Using Modified Concrete Damaged Plasticity. *Eng. Struct.* **2017**, *148*, 23–35. [CrossRef]
41. Henriques, J.; Simões da Silva, L.; Valente, I.B. Numerical Modeling of Composite Beam to Reinforced Concrete Wall Joints. Part II: Global Behavior. *Eng. Struct.* **2013**, *52*, 734–746. [CrossRef]
42. Kyriakopoulos, P.; Peltonen, S.; Vayas, I.; Spyrakos, C.; Leskela, M.V. Experimental and Numerical Investigation of the Flexural Behavior of Shallow Floor Composite Beams. *Eng. Struct.* **2021**, *231*, 111734. [CrossRef]
43. Willam, K.J.; Warnke, E.P. Constitutive Model for the Triaxial Behaviour of Concrete. *Semin. Concr. Struct. Subj. Triaxial Stress.* **1974**, *19*, 30.
44. Petersson, P. Crack Growth and Development of Fracture Zones in Plain Concrete and Similar Materials. *Div. Build. Mater.* **1981**, 1–174.